Acta Materialia 111 (2016) 321–334

Contents lists available at ScienceDirect

Acta Materialia

journal homepage: www.elsevier.com/locate/actamat

Full length article

Multiscale description of carbon-supersaturated ferrite in severely drawn pearlitic wires

Gh. Ali Nematollahi*, Blazej Grabowski, Dierk Raabe, Jörg Neugebauer

Max-Planck-Institut für Eisenforschung, D-40237 Düsseldorf, Germany

ARTICLE INFO

Article history:
Received 24 December 2015
Received in revised form
12 March 2016
Accepted 16 March 2016
Available online 8 April 2016

Keywords:
Multiscale
Dislocations
Carbon
Drag mechanism
Supersaturation
Wire drawing
Pearlite

ABSTRACT

A multiscale simulation approach based on atomistic calculations and a discrete diffusion model is developed and applied to carbon-supersaturated ferrite, as experimentally observed in severely deformed pearlitic steel. We employ the embedded atom method and the nudged elastic band technique to determine the energetic profile of a carbon atom around a screw dislocation in bcc iron. The results clearly indicate a special region in the proximity of the dislocation core where C atoms are strongly bound, but where they can nevertheless diffuse easily due to low barriers. Our analysis suggests that the previously proposed pipe mechanism for the case of a screw dislocation is unlikely. Instead, our atomistic as well as the diffusion model results support the so-called drag mechanism, by which a mobile screw dislocation is able to transport C atoms along its glide plane. Combining the C-dislocation interaction energies with density-functional-theory calculations of the strain dependent C formation energy allows us to investigate the C supersaturation of the ferrite phase under wire drawing conditions. Corresponding results for local and total C concentrations agree well with previous atom probe tomography measurements indicating that a significant contribution to the supersaturation during wire drawing is due to dislocations.

1. Introduction

Mechanical properties of steels are strongly influenced by interactions between solute atoms, in particular large interstitials such as C, and dislocations [1,2]. The extended strain field of a dislocation provides C atoms with a driving force to redistribute and to concentrate inside the dislocation core [3,4]. The segregation of C atoms to a dislocation forms a cloud—known as Cottrell atmosphere [2,4]—pinning the dislocation and altering its distortion field. To unpin the dislocation from the Cottrell atmosphere an additional force is required. The pinning/unpinning process results in a change of the mechanical properties of steels. If this change takes place after deformation, it is commonly termed *static strain-aging*. If the change in mechanical properties occurs during the plastic deformation, it is called *dynamic aging* and it constitutes a serious hindrance to the manufacture of steels [1]. Besides controlling the mechanical properties, the presence and activity of dislocations also influences the thermodynamic stability of interstitial atoms and consequently changes the local composition of phases within steels. While the effect of the C-dislocation interaction on the mechanical properties of steels has been the subject of numerous theoretical and experimental studies [1,2,4–8], the effect on the chemical rearrangement of C within the microstructure of steels has attracted less attention.

A steel with great technological importance that critically depends on C-dislocation interactions are severely deformed pearlitic wires with up to 7 GPa strength [9]. Experimental observations have revealed an exponentially increasing density of dislocations [10–12] and a decomposition of the cementite phase [3,13–21] during the severe plastic deformation. The original stoichiometric C-concentration of 25 at.% in cementite substantially decreases (sometimes even to levels of 10 at.%) and the C atoms redistribute within the ferrite (bcc or α-Fe) lamellae [22]. This redistribution results in a dramatically increased C concentration in the ferrite matrix [3] which is nine orders of magnitude above conventional phase diagram predictions [23]. Several authors [17,24,25] have suggested that there is a correlation between C-dislocation binding energy and the decomposition of cementite. In particular, it has been assumed [3,10] that the C excess atoms from the cementite decomposition are accommodated in the vicinity of dislocations in bcc iron, but so far a quantitative analysis has been lacking. In this

* Corresponding author.
E-mail address: a.nematollahi@mpie.de (Gh.A. Nematollahi).

http://dx.doi.org/10.1016/j.actamat.2016.03.052

study, we therefore present a quantitative multiscale investigation of the role of C-dislocation interactions on the experimentally observed ferrite supersaturation in severely deformed pearlitic microstructures.

The accumulation of C in ferrite is generally assumed to be enhanced by kinetic processes during the severe plastic deformation, in particular due to a dislocation-driven transfer of C atoms from the cementite/ferrite interface into the ferritic layers [3,10,13,25]. Two main dislocation-based scenarios for transporting C atoms from ferrite–cementite interfaces into the ferrite region have been proposed:

- **Pipe diffusion mechanism:** Sauvage et al. [25] have proposed that dislocations located in the ferrite phase and/or crossing the ferrite–cementite interface act as accelerated paths (i.e., pipes) for C diffusion from cementite to the trap sites (e.g., grain boundaries) in ferrite. This idea is based on the assumption that the C migration energy profile is disturbed in the vicinity of a dislocation due to core reconstructions resulting in modified C diffusion barriers. In particular, it is believed [26,27] that diffusion in the core region of dislocations where atoms have a different coordination should be faster than in the bulk region.
- **Drag mechanism:** Li et al. [3,22] have suggested that dislocations propagating from the ferrite–cementite interface into the ferrite phase (either by bulging or by the Frank-Read mechanism) can collect C atoms from cementite and drag them into ferrite. For this drag mechanism to apply, it is necessary that two kinetic phenomena—the diffusion of C atoms and the motion of dislocations—occur with rates in the same order of magnitude. Therefore this mechanism is probable either at sufficiently high temperatures, when C diffusion is fast, and/or at relatively low strain rates, when the dislocation velocity is low [8].

Both mechanisms critically depend on the mobility of the C atoms in the vicinity of dislocations. In this work, computer simulations are used to investigate the effect of the dislocation strain field on the stability and mobility of C.

To study these mechanisms requires simulation techniques that capture C diffusion events and also the motion of dislocations in agreement with experiments. The drag of C atoms by dislocations has been previously studied using molecular dynamics simulations [8]. However, since the molecular-dynamics modeling technique is presently not capable to simulate the time scales for realistic strain rates, typical simulations are performed at strain rates much greater than the ones applied in experiments and at rather high temperatures to accelerate C diffusion. In the present study, a multiscale simulation approach—based on atomistic simulations and a discrete diffusion method—is used to overcome the typical limitations of molecular dynamics simulations and thus to study possible dislocation-based mechanisms involved in the decomposition of cementite under realistic conditions.

In our multiscale modeling approach, the information about C stability and mobility in the vicinity of a dislocation is obtained from atomistic simulations and is transferred as input to a diffusion equation. This allows to overcome the time and length scale limitations of atomistic simulations yet preserving the relevant atomistic information when predicting the target quantities. In particular, we calculate C-dislocation interactions using an embedded atom method (EAM) potential and we use the nudged elastic band (NEB) technique in conjunction with the EAM potential to calculate the migration behavior of C in the vicinity of a screw dislocation. In a final step, we use the atomistic information to study the C transport in the core of a moving screw dislocation by solving the discrete diffusion equation in the vicinity of the dislocation.

2. Methodology

2.1. C-dislocation interaction

The Fe–C EAM potential used in the present work has been developed by Becquart et al. [28]. This binary EAM potential is based on the Fe EAM potential introduced by Mendelev et al. [29] which has been designed with a special focus on properly describing interatomic interactions at small distances. A consequence is a compact core structure of the screw dislocation in bcc iron in good agreement with *ab initio* calculations [28–30] and the correct description of the octahedral (Oh) site as the most stable interstitial position for C in agreement with experimental observations [31]. C diffusion in α-Fe and the tetragonality induced by adding C are also in good agreement with experimental data [28].

Carbon atoms can occupy three different types of Oh interstices in bcc iron. Among the six iron atoms forming an Oh interstitial site, the nearest neighbor iron atoms to the center of the interstice are lying along one of the principle axes of the bcc lattice ([100], [010], and [001] direction) and the remaining four iron atoms are lying on the {110} planes. Inserting a C atom into one of the Oh sites induces a strong tetragonality along the direction of the nearest-neighbor iron atoms, limiting the C solubility in ferrite. In the following, Oh sites will be differentiated based on the direction of the nearest-neighbor Fe atoms, i.e., the Oh site which has nearest neighbors along [100] is called $\mathrm{Oh}_{[100]}$.

Previously we have shown [32] that the presence of an external tensile field dramatically changes the stability of C in an Oh site. Likewise, the strain field of a dislocation changes the stability of C in an Oh site. In order to investigate this effect, we use the following definition for the C-dislocation binding energy:

$$E_{\mathrm{bind}} = E_{\mathrm{dislo+C}} - E_{\mathrm{dislo}} - \mu_{\mathrm{C}}^{\alpha}, \tag{1}$$

where $E_{\mathrm{dislo+C}}$ is the total energy of a system including both a straight dislocation and a C atom in one of the Oh sites, E_{dislo} is the total energy of the system with only a straight dislocation, $\mu_{\mathrm{C}}^{\alpha}$ is the chemical potential of C taken to be

$$\mu_{\mathrm{C}}^{\alpha} = E_{\alpha\mathrm{Fe+C}} - E_{\alpha\mathrm{Fe}}, \tag{2}$$

with $E_{\alpha\mathrm{Fe+C}}$ the total energy of bulk Fe with a C interstitial in an Oh site and with $E_{\alpha\mathrm{Fe}}$ the total energy of a perfect bcc Fe lattice. Based on the definition in Eq. (1), a positive binding energy indicates that the two defects, C and the dislocation, repel each other, and a negative one indicates that they attract each other. As an extension to Eq. (1), we will also compute

$$E_{\mathrm{bind}}(\varepsilon_{\mathrm{el}}) = E_{\mathrm{dislo+C}}(\varepsilon_{\mathrm{el}}) - E_{\mathrm{dislo}}(\varepsilon_{\mathrm{el}}) - \mu_{\mathrm{C}}^{\alpha}, \tag{3}$$

in order to investigate the impact of an externally applied elastic strain, $\varepsilon_{\mathrm{el}}$, corresponding to a uni-axial strain along the [100] direction for a C atom being placed in one of the $\mathrm{Oh}_{[100]}$ sites.

In all simulations, a screw dislocation is introduced in the center of a simulation box with dimensions of $145 \times 139 \times 7.4$ Å^3 by displacing atoms according to the anisotropic elasticity description of a line defect in crystalline materials. In particular, the analytical expression developed by Hirth et al. [33] is used for implementing the dislocation into the supercell. During the following atomic relaxation (performed within the LAMMPS code [34]), an outer layer of ≈10 Å thickness in all directions perpendicular to the dislocation line is kept fixed to reproduce the extended strain field of the dislocation as obtained from linear elasticity theory. The boundary conditions along the dislocation line for all simulations

are considered to be periodic. After relaxation of the pure Fe dislocation, a C atom is inserted in one of the Oh sites in the vicinity of the dislocation and the system is relaxed with the same boundary conditions. The cell size in the direction where the supercell experiences periodic boundary conditions is chosen based on convergence tests to ensure that finite size effects are eliminated. In particular, the tests show that a supercell size of $3b$ (with $b = 2.47$ Å the length of the Burger's vector) along the dislocation line ensures that a bowing of the dislocation does not occur, and that C–C interactions are minimized.

Previous studies [30,35–37] have shown that three different core configurations exist in bcc iron: the easy-core, hard-core, and the split-core configuration. The easy-core configuration is obtained by centering the dislocation line at the gravity center of a triangle formed by iron atoms from three successive (111) planes (see Fig. 1). In the perfect bcc structure, the stacking of (111) planes creates a helical structure along the [111] direction [Fig. 1(b)]. The iron atoms in the easy-core configuration are displaced so that the helicity of the iron atoms in the original bcc lattice is locally reversed around the dislocation line [Fig. 1(c)]. The hard-core configuration is obtained by reversing the Burger's vector of the easy-core configuration, which results in the displacement of the three iron-atom-columns to the same altitude with respect to the [111] direction [30,35–37]. In the split-core configuration, the dislocation core is centered in the immediate vicinity of an iron atom column [36,37], thus breaking the symmetry and allowing for three variants.

First principles calculations based on density-functional-theory (DFT) [30,36,37] have identified the easy-core configuration as the energetically most stable one for a screw dislocation in bcc iron. The EAM potential used in this work correctly reproduces the DFT result, likewise predicting the easy-core configuration as the most stable one. However, the EAM predicted Peierl's potential between two adjacent easy-core configurations, which determines the kinetics of the screw dislocation, shows deviations from corresponding DFT results [30,36,37]. This discrepancy is related to an inaccuracy in the description of the hard-core and split-core configurations: The EAM predicts that the split-core has a lower energy than the hard-core configuration, while DFT predicts the opposite [30,36]. In the present study, we focus on C binding energies and C migration energies around a static dislocation. The migration barrier for the dislocation itself (i.e., the Peierl's potential) does not explicitly enter our atomistic simulations (the dislocation kinetics entering our multiscale approach only at the diffusion equation stage; Sec. 2.4) and thus, for our purpose the employed EAM potential is a reasonable choice. To quantify this statement we will provide, where possible, a comparison of the present EAM results to a recent DFT investigation of C-dislocation interactions in bcc Fe [38].

2.2. C chemical potential calculations

The C-dislocation binding energy defined in Eq. (1) is referenced with respect to the C formation energy in perfect bcc bulk iron, i.e., a bcc region far away from the dislocation core. In order to properly represent the experimental situation in a pearlitic microstructure, we have to consider that the chemical potential of the C atoms is prescribed by the cementite phase. We therefore also need to calculate the energy cost of putting a C atom from the cementite phase into the perfect bcc phase,

$$E_{\mathrm{form}}^{\mathrm{perf}} = (E_{\alpha\mathrm{Fe+C}} - E_{\alpha\mathrm{Fe}}) - \mu_{\mathrm{C}}^{\mathrm{cem}}, \tag{4}$$

where $E_{\alpha\mathrm{Fe+C}}$ and $E_{\alpha\mathrm{Fe}}$ are defined as in Eq. (1) and where $\mu_{\mathrm{C}}^{\mathrm{cem}}$ is the chemical potential of C in cementite. Eq. (4) could be in principle calculated using the Fe–C EAM potential by Becquart et al. [28] introduced in Sec. 2.1. However, this potential was designed for dilute C concentrations, and is therefore not well suited for describing the high C concentration occurring in the cementite phase. More generally, for the present work an interatomic potential would be needed that can correctly describe the ferrite and cementite phases and likewise the dislocation core in ferrite. To our knowledge, there is presently no potential available satisfying all these criteria. For example, one of the most advanced, recent potentials developed by Baskes et al. [39] using the modified EAM approach can replicate cementite and ferrite and the ferrite-to-cementite transformation, but it has not been designed to simulate the dislocation core structure.

To circumvent this problem we use instead *ab initio* calculations based on DFT which were shown to provide a high accuracy for the FeC system, including the ferrite and the cementite phase [40–42]. Employing DFT calculations for computing $E_{\mathrm{form}}^{\mathrm{perf}}$ is enabled by the fact that the terms entering Eq. (4) can be obtained from rather small simulation geometries, in contrast to the terms related to the dislocation in Eq. (1). In particular, we

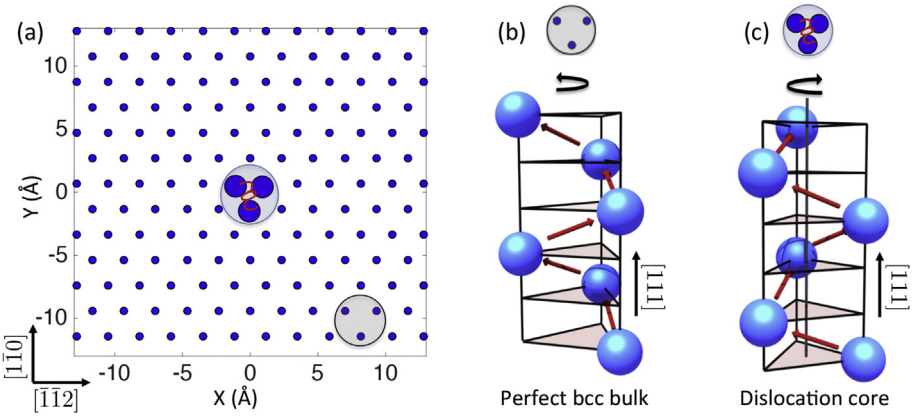

Fig. 1. Arrangement of iron atoms in a screw dislocation in bcc iron. (a) Projection of three (111) planes into a single plane with the dislocation core at the origin of the plot. The three columns of iron atoms nearest to the dislocation center are represented by the big blue dots. (b,c) Schematic representation of the helical arrangement of iron atoms along the [111] direction (b) in perfect bcc bulk and (c) in the core of an easy-core screw dislocation. (For interpretation of the references to color in this figure legend, the reader is referred to the web version of this article.)

use a supercell with 54 Fe atoms and 1 C atom to compute $E_{\alpha Fe+C}$, the conventional cubic unit cell with two atoms for $E_{\alpha Fe}$ (scaled properly to the number of iron atoms in the $E_{\alpha Fe+C}$ supercell), and the primitive cell of cementite with 12 Fe and 4 C atoms for determining μ_C^{cem}.

The total energy of a cementite cell cannot be directly employed for μ_C^{cem}, because of the additional contribution of the cementite Fe atoms. We therefore use instead

$$\mu_C^{cem} = \frac{1}{4}E_{cem} - 3E'_{\alpha Fe}, \tag{5}$$

where E_{cem} is now the total energy of a primitive cementite cell and $E'_{\alpha Fe}$ is the total energy of a perfect α-Fe bulk, scaled per single Fe atom. Eq. (4) together with Eq. (5) correspond to the process of cementite decomposition into a ferrite phase with C interstitials.

As an extension to Eqs. (4) and (5) we will also compute the strain dependent formation energy

$$E_{form}^{perf}(\varepsilon_{el}) = [E_{\alpha Fe+C}(\varepsilon_{el}) - E_{\alpha Fe}(\varepsilon_{el})] - \left[\frac{1}{4}E_{cem} - 3E'_{\alpha Fe}(\varepsilon_{el})\right], \tag{6}$$

where, as indicated, the terms related to the ferrite phase are calculated under an applied elastic strain ε_{el}, corresponding to a uni-axial strain along the [100] direction for a C atom being placed in an $Oh_{[100]}$ site. Calculating Eq. (6) by using DFT is straightforward and guarantees high accuracy. In particular, a uni-axial elastic strain is induced by expanding the corresponding supercell dimension while relaxing the other two perpendicular dimensions, with the atomic coordinates allowed to fully relax.

The DFT calculations are performed employing the projector augmented wave (PAW) method [43] within the Vienna Ab-initio Simulation Package (VASP) [44,45] in combination with the provided PAW potentials [46]. For Fe we use a PAW potential with a valence of $3d^6 4s^2$ and for C with a valence of $2s^2 2p^2$. For the exchange-correlation energy, the generalized gradient approximation within the parameterization proposed by Perdew, Burke and Ernzerhof [47] is used. The cutoff energy for the plane wave expansion of the wave functions is set to 400 eV and the k-point meshes are set to $8 \times 8 \times 8$ for the Fe supercell with a C interstitial, $18 \times 18 \times 18$ for the pure Fe unit cell, and $13 \times 12 \times 9$ for cementite, providing well converged results also for the strained systems. Further, the Methfessel-Paxton scheme [48] with a broadening parameter of 0.2 eV is utilized to smoothen the sum over the occupied electronic states.

2.3. C migration energy calculations

To study the migration energy profile of C in the vicinity of a screw dislocation, we again resort to the Becquart EAM potential [28] (cf. Sec. 2.1) in conjunction with the NEB method [49] including an improved tangent calculation [50] and climbing image procedure [51]. Employing the NEB method allows us to compute the minimum energy path of a C atom jumping from one Oh site in the vicinity of the dislocation to another one in the immediate neighborhood of the original Oh site. For each NEB calculation, 24 intermediate replicas are produced by a linear interpolation between the relaxed supercells including the dislocation and the C atom in the two adjacent Oh sites. The same boundary conditions and supercell size as described in Sec. 2.1 are also used for the migration calculations. A spring constant of 10 eV $Å^{-2}$ is employed to connect the replicas together during the NEB calculations and the "Fire" algorithm as implemented in the LAMMPS package [34] is used to minimize the NEB set-ups.

2.4. C diffusion calculations for moving dislocations

For investigating C diffusion along with a moving dislocation at dislocation velocities corresponding to realistic strain rates, molecular dynamics simulations cannot be applied due to time scale limitations. Instead, we employ for that purpose harmonic transition-state-theory [49,52] which takes as input the migration energy profile from the atomistic calculations. Within transition-state-theory, the rates of the reactions are exponentially linked to the barriers between the energy basins in the phase space of a system, and within *harmonic* transition-state-theory the exponential prefactor is approximated by the vibrational frequencies of the initial and transition state [49]. Yoshinaga et al. [53] used these facts to develop a set of equations to solve the diffusion problem for discrete media, called the discrete diffusion method (DDM), which will be used here.

In bcc iron, each Oh site is surrounded by four other Oh sites in its first nearest neighbor shell. When assuming that a C atom can jump from an Oh site into one of these nearest neighbor Oh sites, the rate of jumps from each Oh site to an adjacent one can be calculated by harmonic transition-state-theory. By knowing the rate of all forward and backward jumps to one particular Oh site, one can calculate the time dependence of the C occupation on that Oh site by [54]

$$\frac{\partial x_i}{\partial t} = \sum_{j=1}^{4}\Big\{x_j\,(1-x_i)\,\nu_0\,\exp\Big[-E_{barrier}^{j\to i}\Big/(k_B T)\Big] - x_i\,(1-x_j)\,\nu_0\,\exp\Big[-E_{barrier}^{i\to j}\Big/(k_B T)\Big]\Big\}, \tag{7}$$

where t is the time, x_i and x_j are the C occupations of Oh sites i and j, ν_0 is the vibrational attempt frequency of a C atom in an Oh site, $E_{barrier}^{j\to i}$ and $E_{barrier}^{i\to j}$ are the energy barriers of C migration from site j to i and *vice versa*, and where k_B is the Boltzmann constant and T the temperature. In Eq. (7) the usual exponential prefactor of harmonic transition-state-theory [49] is approximated by the dominant contribution given by the attempt frequency of the C atom. This attempt frequency ν_0 is related to the diffusion pre-factor D_0 via $\nu_0 = 6D_0/a^2$ [55], where a is the bcc iron lattice constant. We use $D_0 = 1.67 \times 10^{-3}$ cm^2/s and $a = 2.86$ Å [55,56] resulting in $\nu_0 = 1.2 \times 10^{13}$ 1/s. The energy barriers in Eq. (7) are obtained by the aforementioned NEB calculations. The difference between $E_{barrier}^{j\to i}$ and $E_{barrier}^{i\to j}$, that differentiates the forward from backward rate of jumps, originates from the difference in the stability of a C atom in site i and j due to the dislocation strain field.

To simulate a moving dislocation, a convection term can be added to Eq. (7) [54] in order to move the reference frame with the dislocation. In the case of a dislocation moving toward the positive direction of the x-axis (right side) with velocity V_{dislo}, the C occupation of the $(j+)'$th Oh site, located to the right of Oh site i, is biased to move to the site i and the C occupation of the i'th Oh site is biased to the $(j-)'$th Oh site, located to the left of site i. Considering such a convectional term, Eq. (7) changes to [54]:

$$\frac{\partial x_i}{\partial t} = \sum_{j=1}^{4}\Big\{x_j\,(1-x_i)\,\nu_0\,\exp\Big[-E_{barrier}^{j\to i}\Big/(k_B T)\Big] - x_i\,(1-x_j)\,\nu_0\,\exp\Big[-E_{barrier}^{i\to j}\Big/(k_B T)\Big]\Big\} + \frac{V_{dislo}}{a/2}\left[x_{j+} - x_i\right]. \tag{8}$$

The elementary gliding step from one Peierl's valley to the next one for a screw dislocation in bcc iron consists in principle of a kink-pair nucleation and the motion of these two kinks away from each

other. *In-situ* electron-microscopy experiments [57,58] showed for example that at high temperatures and low stresses the kink-pair mechanism is the dominant mechanism in pure Fe. Subsequent work [1] revealed that the presence of C atoms shifts the dominance of this mechanism to lower temperatures and higher stresses. However, the resting time between two successive kink-pair nucleation and/or propagation steps—which move the screw dislocation into an adjacent Peierl's valley—is much longer than the time required for each of the individual motion steps (nucleation and propagation). Hence, in the present work, the time needed for the nucleation and propagation of the steps is neglected. It is assumed that the mass transport occurs only in the resting period between the successive jumps.

3. Results and discussion

3.1. C-dislocation interaction energy

The binding energies between a screw dislocation and a C atom in the three sublattices $Oh_{[100]}$, $Oh_{[010]}$, and $Oh_{[001]}$ around the dislocation are shown in Fig. 2(a). The positions of each sublattice can be reproduced by rotating another one by $\pm 2\pi/3$ around the [111] axis (showing out of the plane). In addition, the strain field of the screw dislocation obeys a three-fold symmetry. Hence, also the binding energy between the screw dislocation and a C atom in one sublattice can be reproduced by a symmetry rotation of any other sublattice energy profile. For example, the C-dislocation binding energies of the $Oh_{[001]}$ sublattice [purple edges in Fig. 2(a)] can be reproduced by rotating the binding energies of the $Oh_{[010]}$ sublattice (gray edges) by $-2\pi/3$ around the dislocation line [111].

A detailed analysis of the energetics shown in Fig. 2(a) reveals that in the out-of-core region (i.e., beyond the dashed black circle) the binding energy is dominated by elastic interactions of the C atom with the strain field of the dislocation. We have explicitly validated this statement by performing continuum theory calculations using linear elasticity in conjunction with Eshelby's inclusion theory [52]. Our conclusion is consistent with the work of Clouet et al. [2] who reported a similar agreement between C-dislocation binding energies obtained by an EAM approach and continuum modelling. Recent DFT calculations support the EAM results. Hanlumyuang et al. [5] used DFT to calculate indirectly the interaction of a C atom with the strain field of a dislocation by employing a strained bcc iron system. Their comparison between the electronic structure and the continuum description reveals that elastic interactions reflect the DFT computed C-dislocation binding energies well for C atoms located outside of the dislocation core.

Within the dislocation core [inside the dashed black circle in Fig. 2(a)] our results reveal that the situation changes significantly. Continuum theory breaks down and core relaxation effects—which can be observed only by atomistic simulations—dominate the binding energy profile. There is a substantial number of Oh sites where the stability of the C atom is considerably increased [blue dots in Fig. 2(a)]. The strongest C-dislocation binding energy is −0.42 eV, and there are 24 such strongly binding Oh sites per nm of the dislocation line. The strong atomic relaxations also lead to a loss of the original bcc crystal symmetry inside the dislocation core. Our results are qualitatively consistent with a recent DFT study by Ventelon et al. [38] who showed for a few specific Oh sites that a C atom is strongly bound and that it leads to local reconstructions inside the dislocation core. Their structural analysis revealed that when a C atom is placed into an Oh site in the vicinity of the dislocation core, the dislocation absorbs the C atom and relaxes towards a hard-core configuration [38]. The exact geometrical details of this DFT predicted relaxation are not reproduced by the present EAM potential, possibly due to its deficiency in describing the hard-core configuration as mentioned in Sec. 2.1. In terms of the C-dislocation binding energy, we observe a factor of two discrepancy for the most favorable site: DFT yields −0.8 eV [38] *versus* −0.42 eV for the EAM potential. Below we will investigate the impact of this deficiency on the C occupancy.

The C binding energy in Fig. 2(a) is defined with reference to an ideal, unstrained ferrite bulk. In a real steel, however, the reference is given by the cementite phase of the pearlitic microstructure. To take this properly into account, we need to compute the formation

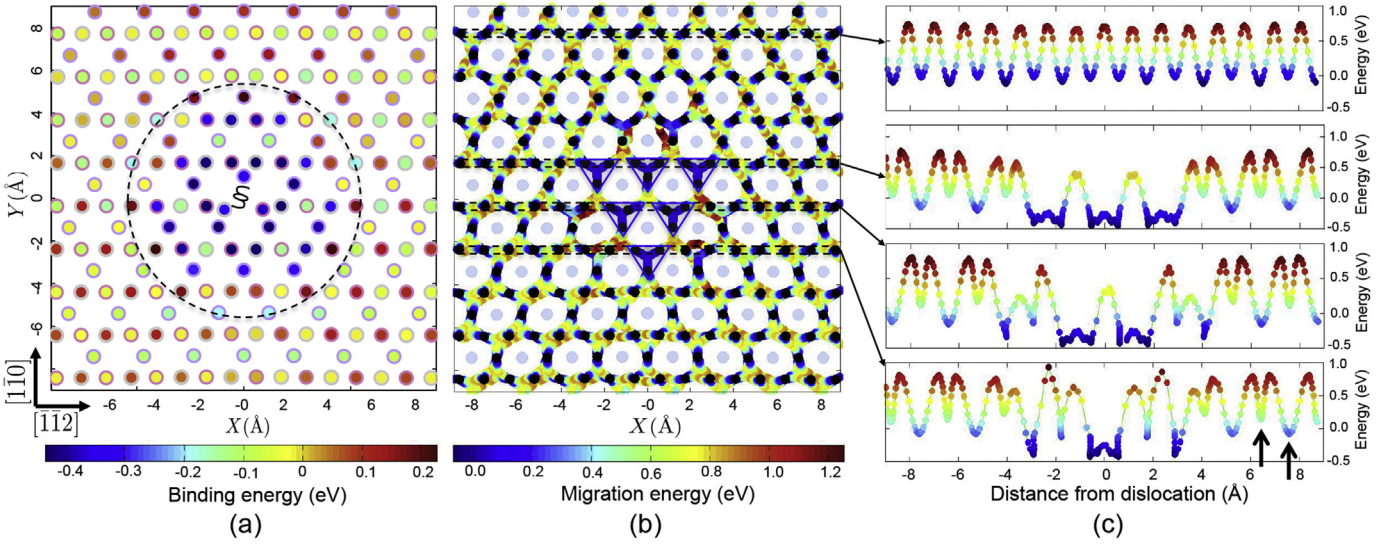

Fig. 2. (a) EAM computed C-dislocation binding energies of Oh sites in the vicinity of a screw dislocation in bcc iron. The dislocation is located at the origin and the dislocation line is perpendicular to the plot. The color of the circles' interior indicates the binding energy associated with the Oh interstices and the color of their edges represents the sublattice type: gray stands for $Oh_{[100]}$, pink for $Oh_{[010]}$, and purple for $Oh_{[001]}$. The large dashed circle indicates the core region. (b) EAM computed minimum energy paths of C migration in the vicinity of a screw dislocation [located as in (a)]. The black dots represent the projection of the Oh sites to the (111) plane while the colored dots between them show the migration barriers of the minimum energy paths calculated by the NEB technique. The light blue dots indicate the iron atoms' positions. The blue triangles indicate the *"high-mobility zone"*, where the C diffusion barriers drop to ≈0.2 eV which is significantly lower than the C diffusion barrier in perfect bcc bulk of 0.86 eV. (c) C diffusion barriers along the [$\bar{1}$12] direction at various distances to the dislocation core as indicated by the black dashed lines in (b). All energies in (a), (b), and (c) are referenced with respect to the C formation energy in perfect bcc bulk. (For interpretation of the references to color in this figure legend, the reader is referred to the web version of this article.)

energy of a C atom with respect to a chemical reservoir corresponding to the cementite phase. As mentioned in Sec. 2.2, we cannot employ the EAM potential for that purpose and we therefore extend our multiscale approach to *ab initio* based DFT calculations. Specifically, we compute the strain dependent formation energy of a C atom in a perfect ferrite phase (i.e., no dislocation) with respect to the cementite phase according to Eq. (6).

Fig. 3 shows that for zero elastic strain we obtain a C formation energy of 0.4 eV. This value is considerably lower than the C formation energy of 1.2 eV found in Ref. [32] where a C vacancy was assumed to form inside the cementite phase. Here, we find that an energetically more favorable situation is the decomposition of the cementite phase according to Eq. (5). This reduction in the C formation energy (i.e., from 1.2 to 0.4 eV) is of great significance because it brings the C formation energy close in absolute value to the C-dislocation binding energies in the core of the dislocation. The resulting situation is illustrated by a schematic C formation energy profile in Fig. 4. Taking a C atom (black ball) from the cementite phase (right part of Fig. 4) into an unstrained perfect bcc iron bulk costs 0.4 eV. But, moving the C atom into the dislocation core (indicated by the dip in the black solid curve) the system gains energy (−0.42 eV or −0.8 eV considering EAM or DFT [38] results, respectively), compensating the initial C formation energy. Thus, in equilibrium, it is energetically favorable to decompose parts of the cementite phase, transform it into ferrite, and bring the corresponding C atoms into the core of dislocations.

During the drawing process the system is exposed to considerable strains which affect the C binding energy profile. Our DFT results in Fig. 3 show that, for example, an elastic strain of 2% along the [100] direction has a dramatic effect on the C formation energy of the $Oh_{[100]}$ site in the perfect ferrite phase, lowering it almost to zero. Such strain magnitudes are not unrealistic during the drawing process, since they correspond to elastic distortions associated with yield stresses conventionally achieved in such materials (see upper X-axis in Fig. 3), which can even reach values above 6 GPa [60]. In terms of the schematic C formation energy profile in Fig. 4, the application of elastic strain results in a lowering of the C energy profile in the ferrite phase as indicated by the red dashed curve.

Utilizing Eq. (3), we have performed explicit EAM simulations to quantify the effect of strain on the binding energy profile around the dislocation. Specifically, we applied a strain of ε=0.5% along the [100] direction for a supercell with a dislocation and a C atom

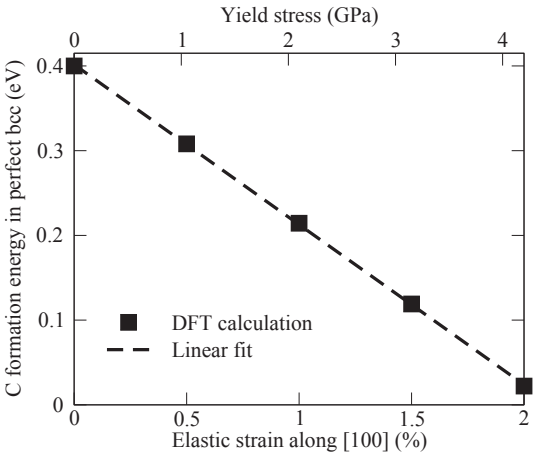

Fig. 3. DFT computed C formation energy in an $Oh_{[100]}$ site in a perfect ferrite phase (i.e., no dislocation present) as a function of uni-axial elastic strain along the [100] direction with cementite as the chemical potential according to Eq. (6). The upper X-axis indicates at which yield stresses the corresponding elastic strains can in principle be achieved. The yield stresses were obtained using $\sigma=\varepsilon_{el}E$, where ε_{el} is the elastic strain and $E=210$ GPa the Young's modulus of iron.

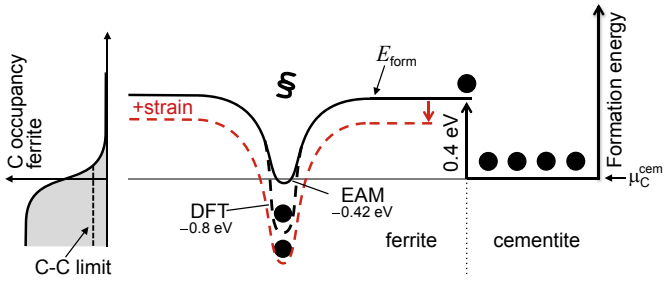

Fig. 4. Schematic of the C binding energy profile in a deformed pearlite microstructure. A ferrite phase including a dislocation (indicated by the section symbol) and a cementite phase populated with carbon atoms (black balls) are shown. A formation energy of 0.4 eV is required to bring a C atom from the cementite phase (chemical potential μ_C^{cem}) into the perfect bcc/ferrite phase (DFT result). Inside the dislocation core the formation energy is significantly reduced due to the C-dislocation binding energy. The black solid line indicates the EAM results for the C-dislocation binding energy (strongest binding is −0.42 eV) and the dashed black line the DFT results from Ref. [38] (−0.8 eV). The red dashed curve indicates the change in the binding energy in ferrite upon application of strain (with respect to the DFT curve). To the left, the C occupation profile inside the ferrite phase corresponding to the Fermi-Dirac function in Eq. (9) is shown. The vertical dashed line labeled "C–C limit" indicates that the Fermi-Dirac function is only occupied until this limit due to C–C interactions [59]. (For interpretation of the references to color in this figure legend, the reader is referred to the web version of this article.)

placed subsequently in all of the $Oh_{[100]}$ sites. The decrease in the binding energy far away from the dislocation is −0.16 eV, in good agreement with the DFT computed value of −0.1 eV (Fig. 3). In Fig. 5 the results for $Oh_{[100]}$ sites closer to the dislocation are shown, with the red dashed line indicating a perfectly constant shift in binding energy corresponding in value to the decrease in the bulk region. We see that the decrease in the binding energy in the out-of-core region (gray circles) is closely distributed around the red dashed line. Inside the core region (green squares), part of the binding energies shows a similar distribution around the red dashed line. There is also a fraction of sites experiencing a stronger decrease as indicated in Fig. 5. Thus under strain, even more energetically

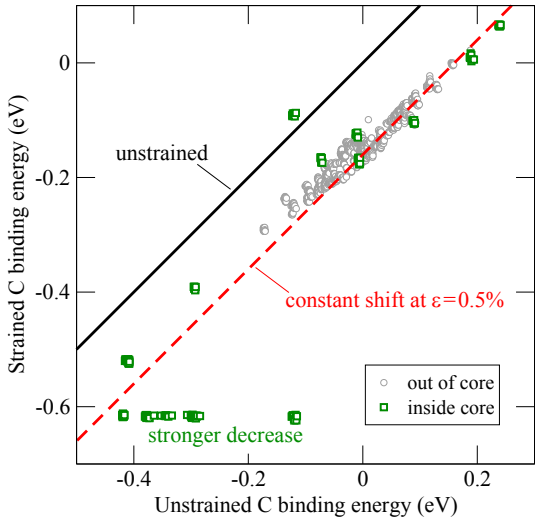

Fig. 5. EAM computed C binding energies of $Oh_{[100]}$ sites around a screw dislocation under an applied elastic strain of ε=0.5% in the [100] direction, as a function of the unstrained binding energies. The black solid line labeled 'unstrained' provides a reference line on which all points would lie if the strain was reduced to zero. The red dashed line indicates a perfectly constant shift with strain, at a value of −0.16 eV corresponding to the shift in C binding energy in the perfect bulk at ε=0.5% for the used EAM potential. The values of the strained binding energies are grouped into the out-of-core region (gray circles) and core region (green squares) according to the separation in Fig. 2(a). (For interpretation of the references to color in this figure legend, the reader is referred to the web version of this article.)

favorable C sites become available around the dislocation (cf. red dashed line in Fig. 4).

At finite temperatures the equilibrium C occupation x in the ferrite phase is determined by the Fermi-Dirac distribution

$$x(\varepsilon_{el}) = \left(\exp\left[\frac{E_{form}(\varepsilon_{el})}{k_B T}\right] + 1\right)^{-1}, \quad (9)$$

where $E_{form}(\varepsilon_{el})$ is the strain dependent formation energy of a C atom in the ferrite phase including a dislocation, referenced with respect to the cementite chemical potential μ_C^{cem} (as indicated in Fig. 4). An example for such a distribution function is shown in the left part of Fig. 4. In applying the Fermi-Dirac function to occupy the dislocation core where the formation energy becomes negative, it is crucial to consider the influence of C–C interactions to prevent unrealistically high C concentrations. Inside the dislocation core, where C-dislocation binding energies are strong, the C occupation obtained from Eq. (9) is close to 1. This would require three carbon atoms per one iron atom within a radius of a few angstrom around the dislocation line, leading to much higher concentrations than experimentally observed [59]. Veiga et al. [59] were able to resolve this issue by estimating the impact of C–C interactions on the C concentration inside the dislocation core by explicit atomistic calculations. They successfully modeled the C distribution in a Cottrell atmosphere as a function of the C concentration in the ferritic matrix and showed that within a screw dislocation core the maximum C occupancy per sublattice site is much smaller than 1. It can reach only values of 0.04, which corresponds to a maximum C concentration of 12 at.%. Such a C occupancy limit due to C–C interactions is indicated in Fig. 4 by the vertical dashed line, essentially cutting off the Fermi-Dirac distribution function already at rather small values.

In Sec. 4 below, we will utilize Eq. (9) together with the C–C limit to derive local and total C concentrations in the ferrite phase that can be used to analyze experimental data. For that purpose it will prove useful to estimate the error in the C occupancy introduced by the too weak EAM C-dislocation binding energies as compared to DFT. Taking the strongest EAM binding energy of −0.42 eV, the total C formation energy is slightly negative $E_{form} = -0.02$ eV (cf. Fig. 4) which at room temperature leads to $x = 0.68$. Taking instead the strongest DFT binding energy −0.8 eV [38], we have $E_{form} = -0.4$ eV leading to full occupancy $x = 1$, i.e., considerably higher than for the EAM case. However, due to the above discussed C–C interactions the C occupancy cannot actually reach such high values and is cut off already at 0.04 in both cases. More generally, we can state that, due to C occupancy limit, the C occupancy is invariant to changes in E_{form} as long as they happen in the range below $E_{form} = k_B T \ln(1/0.04 - 1) = 0.08$ eV (at room temperature).

3.2. Carbon diffusion energetics around the dislocation

In Sec. 3.1 we have shown that in thermodynamic equilibrium the dislocation acts as an energetic sink attracting C atoms from the cementite phase. We now extend the analysis towards a kinetic treatment and start with investigating the C diffusion barriers between neighboring interstitial sites around the dislocation as shown in Fig. 2(b) and (c).

We observe that several angstrom away from the dislocation core [e.g., upper panel in Fig. 2(c)] the C diffusion energy profile is regular and the barriers are close in value to the perfect bcc bulk diffusion barrier of 0.86 eV. This value is in perfect agreement with the DFT derived value of likewise 0.86 eV and with the experimental value of 0.87 eV [55]. As we approach the core region the diffusion profile becomes irregular and the barrier energies are modified. Partially, the changes in the barriers can be understood by local differences in the binding energies of the three sublattices $Oh_{[100]}$, $Oh_{[010]}$, and $Oh_{[001]}$. These binding energy differences, exemplified by the two black arrows in Fig. 2(c), originate in the different local response of each sublattice to the dislocation strain field. One immediate consequence of these local variations in the binding energy is that the energy barriers become asymmetric with respect to a forward or backward jump.

In the direct neighborhood of the dislocation center the diffusion energy profile is highly modified compared to the perfect bulk lattice. This modification is a consequence of atomistic core relaxation effects and is invisible in a continuum description. Of particular importance is the region highlighted in Fig. 2(b) by the blue triangles, hereafter called *"high-mobility zone"*, where the diffusion barriers drop to ≈ 0.2 eV which is significantly lower than the C diffusion barrier in perfect bcc bulk of 0.86 eV. These low diffusion barriers indicate that C atoms can be exceptionally mobile in the vicinity of the dislocation center. The implications of the *high-mobility zone* on the pipe diffusion mechanism and drag mechanism will be discussed in the following sections.

3.3. Pipe diffusion along the screw dislocation

One of the proposed mechanisms for C redistribution in severely deformed pearlitic steel suggests that C atoms exploit dislocations to diffuse easily from the cementite/ferrite interfaces into the ferrite region [25]. As shown in Sec. 3.2, the diffusion barriers of C in the vicinity of a screw dislocation are significantly decreased in the region close to the dislocation center, which might be considered as an evidence of fast pipe diffusion. However, such a consideration is too premature since low energy barriers are only a necessary condition for pipe diffusion, but not a sufficient one. In addition, the geometrical direction of the minimum energy path is of critical importance considering the fact that the concept of pipe diffusion refers to accelerated jumps along the dislocation line. Hence, to prove that the pipe diffusion mechanism is operational during the cementite decomposition, it needs to be shown that the low energy barriers in the *high-mobility zone* are aligned with the screw dislocation line.

As shown in Fig. 6(a), C atoms (green spheres) diffuse in bulk bcc iron by jumping from one Oh site to another one along ⟨100⟩ directions [28,61,62]. Therefore, to diffuse along the [111] screw dislocation direction by a distance of a Burger's vector, a C atom needs to jump three times. All jumps in bulk bcc iron are equivalent and have the same angle of 54.7° with respect to the [111] direction. However, in the strain field of the dislocation, the Oh sites' relative positions deviate from the perfect bulk arrangement and, in consequence, the angles between the directions of jumps and the screw dislocation line change. As shown in Fig. 6(b), these changes depend on the average distance, d, between the Oh sites involved in each jump and the center of the dislocation:

- In the region beyond the dislocation core (d>6 Å), the angles between the jump paths and the dislocation line are only slightly influenced by the strain field of the dislocation and are thus close to the perfect bulk value of 54.7° [vertical dashed line in Fig 6(b)]. This observation correlates with the already discussed fact that the energy barriers in this region are likewise close to the perfect bulk value as highlighted again in Fig. 6(c).
- In the high-mobility zone, where the C diffusion barriers are decreased, the angles between the jump paths and the dislocation line deviate significantly from the bulk value. Most of the angles increase with some approaching 80° [Fig. 6(b)]. The corresponding component of the jump paths projected onto the dislocation line [111] becomes shorter than 0.3 Å. This value is much smaller than the component of a C jump along [111] in

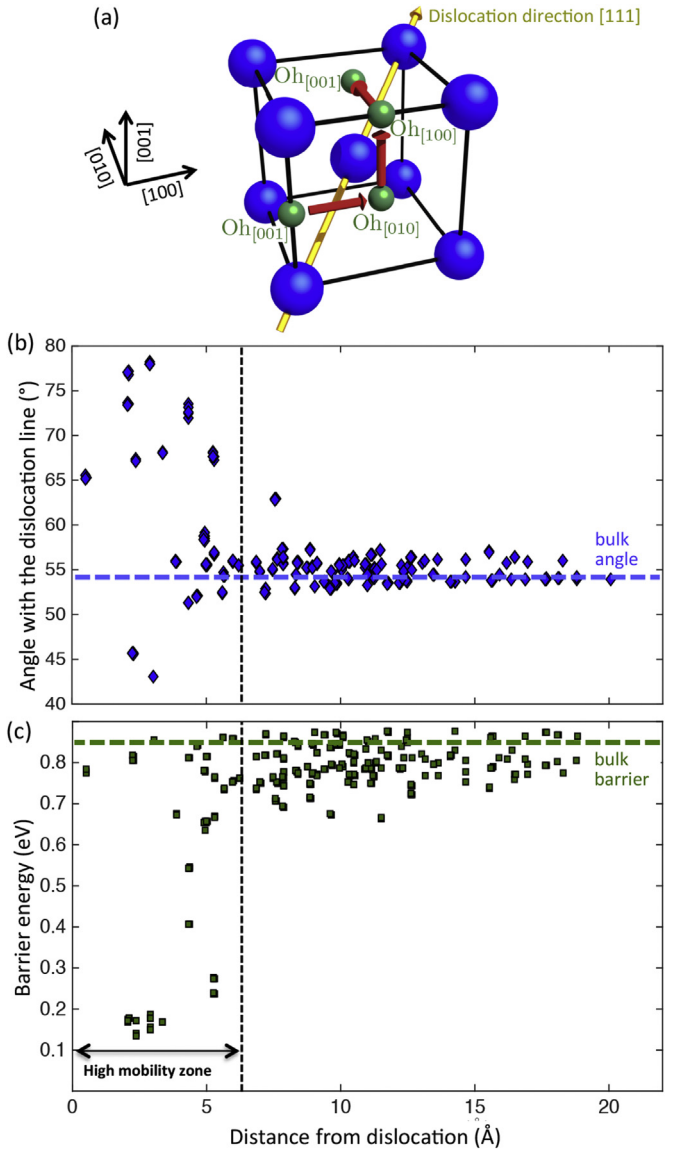

Fig. 6. (a) Schematic of the possible C diffusion paths (red arrows) between the different Oh sublattices in a perfect bcc structure. The screw dislocation direction is also indicated (yellow arrow). (b) Angles between C diffusion paths in the vicinity of a screw dislocation and the dislocation line as a function of the average distance between the Oh sites involved in each jump and the dislocation line. The corresponding angle in perfect bcc iron is 54.7° (blue dashed line). (c) Diffusion barriers corresponding to the jumps in (b). The C diffusion barrier in bulk bcc iron is 0.86 eV (green dashed line). (For interpretation of the references to colour in this figure legend, the reader is referred to the web version of this article.)

perfect bcc iron which is about 0.8 Å. Consequently, the fast diffusion of the C atoms due to the low barrier in the high-mobility zone is predominantly in the plane normal to the dislocation line and not parallel to the dislocation line.

Thus, our results indicate that the jump paths which have a large component along the [111] dislocation line have a high diffusion barrier, and that the low energy paths have only a small component along the dislocation line. Further analysis shows that the low barrier paths observed in the atomistic simulations are not directly linked together along the dislocation line. They do not provide the C atom with an accelerated diffusion path to diffuse along the dislocation line. Therefore, contrary to previous believe [25] pipe diffusion in a screw dislocation, i.e., C diffusion along the [111] dislocation axis, seems inefficient. Note however that, as previously mentioned, the present EAM potential cannot reproduce all details of the reconstruction from the easy-core to the hard-core configuration upon the introduction of a C atom into the dislocation core, as predicted by DFT [38]. Testing the impact of this deficiency requires DFT based C migration barrier calculations inside of the screw dislocation core which are beyond the scope of the present study.

3.4. Carbon dragged by a mobile screw dislocation: atomistic insights

The drag mechanism proposed in Ref. [3] suggests that C atoms are transported by mobile dislocations from cementite into ferrite. Since it has been experimentally observed that dislocations can pass through cementite layers [63] and since we have shown in Sec. 3.1 that there is a strong attractive C binding region in the core, it is in principle possible for dislocations to collect C atoms while passing through the cementite lamella and to redistribute them in the ferrite lamella. However, for such a drag mechanism to apply, the C atoms trapped inside the dislocation core need to diffuse at least as fast as the dislocation moves in order to be able to follow the dislocation (Portevin le Chatelier effect) [8,64]. In this section, we provide a simple and intuitive atomistic analysis of the C migration barriers to examine this possibility, before extending it to a more complex analysis in the next section.

In particular we want to estimate the velocity with which a C atom can follow a moving dislocation. We need for that purpose the C jump frequency at a temperature T over a given barrier E_{barrier} which is given by [49]

$$\nu = \nu_0 \exp\left(-\frac{E_{\text{barrier}}}{k_B T}\right), \tag{10}$$

where ν_0 is the attempt frequency and k_B the Boltzmann constant. Using $\nu_0 = 1.2 \times 10^{13}$ 1/s (see Sec. 2.3), a realistic temperature during wire drawing of 450 K [15], and $E_{\text{barrier}} = 0.2$ eV representing the migration barriers in the *high-mobility zone* [Fig. 6(c)], we obtain ν=6.9 × 10^{10} 1/s. To estimate the velocity we also need the length of a C jump projected onto the dislocation glide plane. In Sec. 3.3 we have shown that in the *high-mobility zone* the C jump direction is normal to the dislocation line. A further analysis of our data shows that the C jump direction inside the *high-mobility zone* is additionally very well aligned with the glide direction of the screw dislocation. The actual length of the jump between two nearest neighbor interstitials is $d = 1.2$ Å and we can thus estimate the C velocity,

$$V_C = d\nu = 8.3 \times 10^{10} \text{Å}/\text{s}\ (= 8.3\ \text{m/s}), \tag{11}$$

with which C atoms can in principle migrate in the dislocation core along the glide plane.

To clarify the significance of V_C, we also need to estimate the relevant dislocation velocity range during wire drawing. The true dislocation velocity distribution is a complex function depending on the microstructural details [65]. For our purpose, it is sufficient to use a simplified estimate based on Orowan's equation for which the average dislocation velocity, V_{dislo}, is proportional to the mobile dislocation density, ρ_{dislo}, and the applied deformation rate, $\dot{\varepsilon}$, as

$$V_{\text{dislo}} = \frac{\dot{\varepsilon}}{b\,\rho_{\text{dislo}}}, \tag{12}$$

where b is the magnitude of the Burger's vector ($b = 2.47$ Å). In severely deformed pearlitic steel, the dislocation density strongly

increases with applied strain. Chen et al. [11] recently obtained $\rho_{dislo} = 8 \times 10^{14} \ldots 10^{16}\ m^{-2}$ by X-ray diffraction measurements. Due to the complex microstructure and strain state within the drawn wire, it is impossible to determine the actual fraction of mobile dislocations. We therefore use the simplifying assumption that all dislocations contribute to the deformation. A reasonable assumption for the strain rate during wire drawing is $\dot{\varepsilon} = 2 \times 10^{-2}\ s^{-1}$ [66], and thus our estimate for the relevant dislocation velocity range during wire drawing is

$$V_{dislo} = 80 \ldots 1000\ \text{Å}/\text{s}. \quad (13)$$

Comparing with Eq. (11) we see that C atoms inside the *high-mobility zone* are several orders of magnitude faster and should thus easily be able to follow the dislocation motion.

Based on this insight, we propose the following simplified phenomenological model of how C atoms could be dragged by a screw dislocation in bcc iron. The black triangles in Fig. 7 are the original positions of the *high-mobility zone*, where as just discussed C atoms are very mobile at wire drawing temperatures. As the dislocation glides from one Peierl's valley to an adjacent one, the triangles move to new positions as indicated in Fig. 7 by the blue triangles. The red dashed triangles indicate one possible intermediate position of the *high-mobility zone* between the two adjacent Peierl's valleys. Assuming that at this intermediate stage the C diffusion barriers are not significantly increased in the *high-mobility zone*, there will be linked paths with low migration barriers available during the dislocation motion so that C atoms can co-migrate with the dislocation.

The model proposed here provides a simple and intuitive atomistic picture of the drag mechanism. It neglects however the actual complexity of the diffusion energy profile in the dislocation core and it treats the coupling between C and dislocation motion on very simple grounds. In the following section we present a more complex and thus more realistic description.

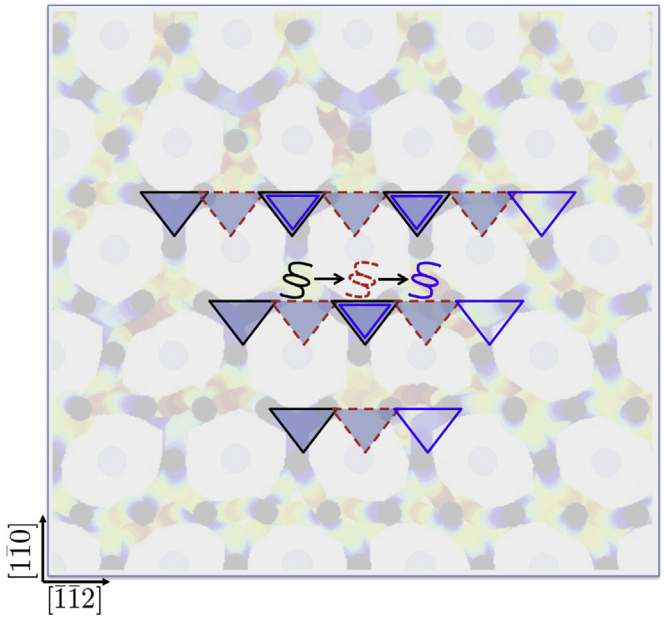

Fig. 7. Schematic of the suggested phenomenological model for a possible C drag mechanism by the core of a screw dislocation. The black section symbol and the black triangles indicate the initial position of the dislocation and the high mobility zone, and the background indicates the corresponding minimum energy paths of C migration [cf. Fig. 2(b)]. The blue section symbol and the blue triangles show the final positions after moving into the next Peierl's valley along the glide direction [$\bar{1}\bar{1}$2], while the dashed red symbols mark one possible position between the two Peierl's valleys. (For interpretation of the references to colour in this figure legend, the reader is referred to the web version of this article.)

3.5. Carbon dragged by a mobile screw dislocation: extension to more realistic conditions

The discussion of C dragged by a mobile screw dislocation will be now extended to a more realistic picture. We present our simulation results based on the discrete diffusion method (DDM; Sec. 2.4) allowing to infer the migration behavior at experimentally relevant time scales. The DDM simulation is informed with the energetics obtained from the atomistic simulations ensuring good quantitative and thus predictive capability.

Fig. 8 shows a representative set of DDM results for a dislocation with a velocity of 100 Å/s at a temperature of 450 K. In Fig. 8(a) (left column) snapshots of the C occupation profile at different times in a plane perpendicular to the dislocation line are shown. In Fig. 8(b) (right column) an averaged C occupation profile obtained by averaging over the Y-axis in Fig. 8(a) at the corresponding times is shown. The simulation has been performed in a moving reference frame so that the dislocation is always located in the origin of the plots in all snapshots. At the starting time $t = 0$ s, the C occupation was homogeneously distributed throughout the cell to a value of 1 at.%. Cross checks for other concentrations revealed the same qualitative behavior as discussed next.

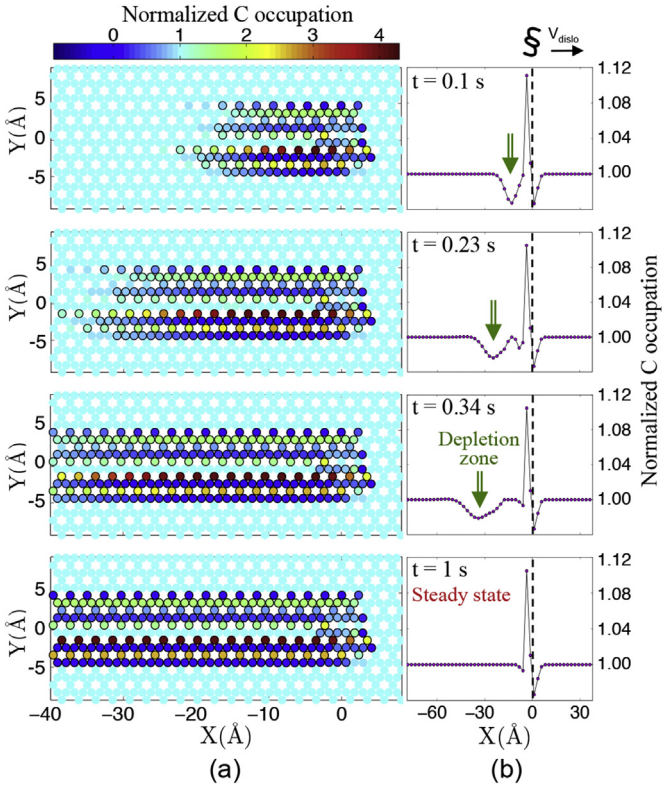

Fig. 8. Time evolution (from top to bottom) of the C occupation profile computed by using the discrete diffusion method (DDM) for a screw dislocation moving at a velocity of 100 Å/s and at a temperature of 450 K. (a) Snapshots in a plane perpendicular to the dislocation line and with the glide direction from left to right. The dislocation is throughout located at (0,0) due to the moving reference frame. The circles represent Oh sites and their color indicates the corresponding C occupation which is normalized with respect to the perfect bulk value far away from the dislocation. (b) Averaged C occupation profiles corresponding to the snapshots in (a). The average has been performed over the Y-axis.

The strong binding of the C atoms to the dislocation core and the low migration barriers in the *high-mobility zone* lead to a redistribution of the C occupation in the vicinity of the moving dislocation already after short simulation times [cf. Fig. 8(a) at a time step of 0.1 s]. The redistribution leads to a rather complex occupation profile which leaves behind a specific footprint of the passing dislocation as time progresses. A simpler picture of the process is obtained from the averaged occupation profiles given in Fig. 8(b). Already after a short simulation time a significant amount of extra C atoms is accumulated in the core as indicated by the peak left to the vertical dashed line. The C atoms responsible for the peak are supplied by a depletion zone located several angstrom behind the dislocation (indicated by the green arrow), i.e., in the region where the dislocation just passed through. As time increases, the depletion zone widens and is left behind the dislocation. Finally, after a time of roughly 1 s, the system reaches a steady-state condition and the averaged occupation profile converges to a fixed shape. In the steady state condition, the number of C atoms left behind the dislocation is balanced by the number of C atoms collected from the front of the moving dislocation.

The amount of C effectively dragged by the dislocation is mainly determined by the peak in the occupation profile at the dislocation core. For an exact determination, also the small depletion zone ahead of the dislocation [Fig. 8(b)] needs to be considered. We therefore integrate the steady-state C occupation within a radius of 10 Å around the mobile dislocation and subtract the bulk concentration of 1 at.% to unveil n_{drag}, the net number of dragged C atoms. The result is shown in Fig. 9(a) as a function of the dislocation velocity and for different temperatures. We observe that more C atoms can be transported by the dislocation either at lower velocities or at higher temperatures. This dependence can be intuitively understood by considering that the drag is controlled by the diffusivity of carbon: At lower dislocation velocities the C atoms have sufficient time to follow the dislocation also at lower temperatures, whereas at higher temperatures they have a sufficiently high mobility to keep up even with faster dislocations.

In order to better understand the generic behavior of the C drag curves, we normalize the velocity axis by $\nu^{\mathrm{C}}_{\mathrm{bulk}}$, the C jump frequency for bulk bcc iron, and the n_{drag}-axis by n^{0}_{drag} corresponding to the number of C atoms dragged by an infinitely slow dislocation. This procedure brings the different curves close together as shown in Fig. 9(b). Very slow dislocation velocities are not accessible due to simulation time limitations. We have therefore constructed a numerically inexpensive one-dimensional model that uses as input the atomistic energetics obtained in the present study [52]. Using this model, we were able to deduce the complete velocity dependence as exemplified by the S-shaped, black solid curve in Fig. 9(b). The curve saturates at a value of 1 for the limit of a stationary dislocation meaning that the complete Cottrell atmosphere can be transported by the dislocation.

In Sec. 3.1 we have stressed the importance of C–C interactions when occupying the static dislocation with C atoms. Here, we cannot directly employ the maximum C occupancy of 0.04 (i.e., 12 at.%) for a static screw dislocation [59] due to the fact that the occupation profile for a moving dislocation (Fig. 8) is completely different from the one for the static dislocation. Nevertheless we can estimate the impact of C–C interactions within the generalized dependence of the C drag curves in Fig. 9(b). To this end we compute the number of C excess atoms for a static dislocation according to Eq. (9) once with the C occupancy limit of 0.04 and once without. The corresponding ratio depends to some extent on the C background concentration and temperature, but a ratio of 20% reflects the impact of C–C interactions rather well. Thus, the number of dragged C atoms for very slow dislocations will converge to the limit indicated by the vertical dashed line in Fig. 9(b). For fast

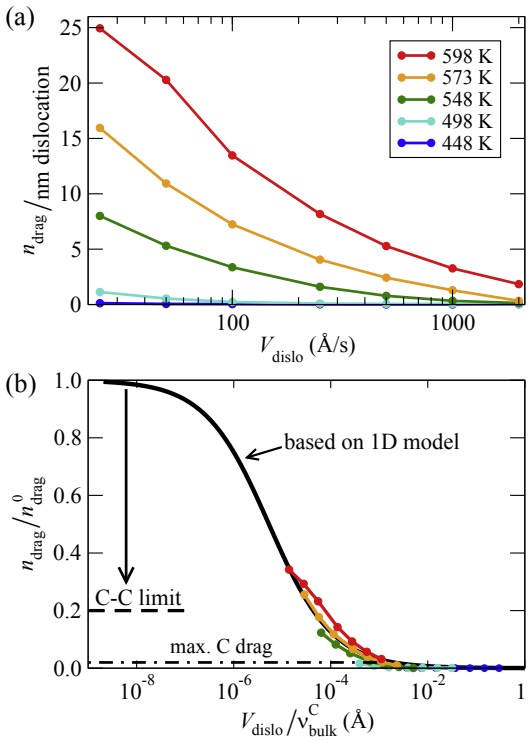

Fig. 9. (a) Number of carbon atoms, n_{drag}, per nm of dislocation line length effectively dragged by a mobile screw dislocation at various dislocation velocities, V_{dislo}, and temperatures. To obtain n_{drag}, steady-state C occupation profiles (as exemplified in Fig. 8 for a specific velocity and temperature) were integrated within a radius of 10 Å around the mobile dislocation and the perfect bulk concentration was subtracted. (b) Generic dependence of the n_{drag}-curves from (a) obtained by normalizing the velocity by $\nu^{\mathrm{C}}_{\mathrm{bulk}}$, the C jump frequency in bulk bcc iron, and by normalizing n_{drag} by n^{0}_{drag}, the number of C atoms dragged by an infinitely slow dislocation. The black solid line is a result for a simplified one-dimensional model [52] illustrating the dependence for very slow dislocation velocities. The vertical dashed line represents the ratio between the number of dragged C atoms calculated according to Eq. (9) once with the C occupancy limit of 0.04 and once without for very slow dislocations. The vertical dash-dotted line shows the maximally possible number of C atoms dragged by a mobile dislocation at wire drawing conditions. (For interpretation of the references to colour in this figure legend, the reader is referred to the web version of this article.)

dislocations or at low temperatures, the number of dragged C atoms will be unaffected by C–C interactions, because the number of dragged C atoms is small for such conditions.

The relevant dislocation velocity range occurring during wire drawing [Eq. (13)] and the respective temperature range [15] are indicated by the horizontal and vertical dashed lines in Fig. 10. The white dashed rectangle in the middle highlights the resulting window of the most probable experimental conditions. To see which numbers of C atoms can be dragged in this window, we overlay contour lines (blue, red, and black solid curves) extracted from the C drag curves of Fig. 9. We observe that from about 0.01 to 1 C atoms per nm of dislocation line can be dragged within the experimental window. As shown in Fig. 9(b) by the dashed-dotted line, these values are sufficiently small to not be affected by C–C interactions. Nevertheless, these values can be relevant for explaining the experimentally observed ferrite supersaturation [9]. To support this statement we estimate the increase of the C concentration in ferrite based on the computed C drag results.

To this end, we approximate the C concentration increase in ferrite by

$$\Delta c = n_{\mathrm{drag}}\, n_{\mathrm{cross}}\, \rho_{\mathrm{disl}}\, \vartheta_{\mathrm{Fe}}, \tag{14}$$

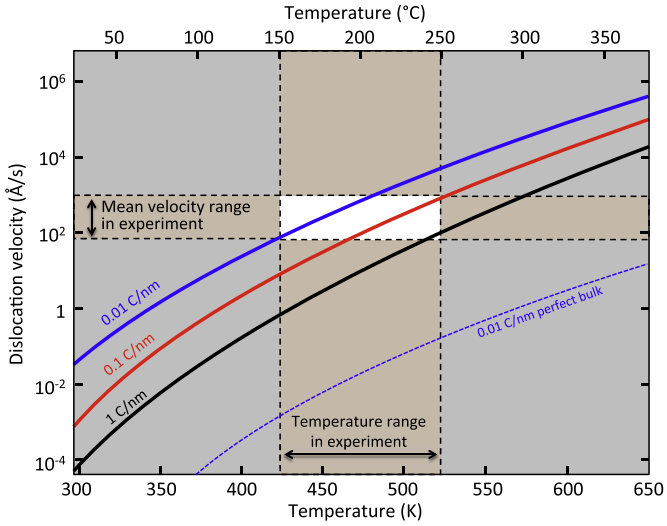

Fig. 10. Contour lines (blue, red, black) of a fixed amount of C atoms dragged by a mobile screw dislocation in the 2D parameter space of dislocation velocity and temperature. The experimentally relevant velocities and temperatures are indicated, resulting in a window (white rectangle in the middle) of the most probable experimental conditions. The dashed blue line indicates a result obtained by assuming the perfect bulk C diffusion barrier within the dislocation core, i.e., by neglecting the effect of the *high-mobility zone*. (For interpretation of the references to colour in this figure legend, the reader is referred to the web version of this article.)

where n_{drag} is the number of C atoms dragged by a dislocation, n_{cross} is the number of times a dislocation segment with a length of 1 nm crosses a cementite lamella, ρ_{disl} is the density of dislocations, and ϑ_{Fe} is the atomic volume of Fe in the bcc phase. We use in particular $n_{drag} = 0.5$ C/nm, $\rho_{disl} = 8 \times 10^{14}$ m^{-2} [11], and $\vartheta_{Fe} = 11.3$ Å^3. Further, we approximate $n_{cross} = \bar{x}(\varepsilon)/l$, where $\bar{x}(\varepsilon)$ is the average dislocation displacement for a given increase in total plastic wire drawing strain ε, and l is the width of a ferrite + cementite lamella. To estimate $\bar{x}(\varepsilon)$ we multiply Orowan's equation, Eq. (12), with time on both sides to obtain $\bar{x}(\varepsilon) = \varepsilon/(b\,\rho_{dislo})$. Using ε=2 and a corresponding lamella thickness $l = 30$ nm [3] we obtain $n_{cross} = 337$ and eventually $\Delta c = 0.15$ at.%. In Sec. 4 we will show that at the same drawing strain of ε=2 the experimental C background concentration in the ferrite phase agrees well with the here estimated value.

It is worthwhile stressing that the *high-mobility zone* with the low diffusion barriers of 0.2 eV is critical in the above calculation. Assuming for comparison a perfect bulk C diffusion barrier of 0.86 eV within the dislocation core (keeping however the strong C-dislocation binding energies), the contour lines in Fig. 10 shift to significantly lower velocities as exemplified by the blue dashed curve. Within the range of experimental dislocation velocities and temperatures, $n_{drag} = 0.006$ and thus we obtain a negligible concentration increase $\Delta c = 0.002$ %.

4. Analysis of C supersaturation during wire drawing

In Sec. 3 we have applied a multiscale theoretical approach to identify the impact of C-dislocation interactions during pearlitic wire drawing from a thermodynamic and kinetic perspective. In essence, we have shown that a screw dislocation offers C interstitial sites in the dislocation core with energies lower than in cementite and that there is also an efficient drag mechanism of C by the dislocation. We will now establish the connection to the experimentally observed C supersaturation of the ferrite phase during wire drawing [3]. Thereby, we will be able to validate our theoretical data, and we will also gain a deeper understanding of the experimental observations.

In Ref. [3] a significant increase of the C concentration was observed in the ferrite phase with increasing wire drawing strain. The overall C concentration in the bulk phase was found to be far above the equilibrium limit of ferrite, with even stronger accumulations in some local regions. In Fig. 11 we have replotted a representative result from Ref. [3] (green colored data set) showing a one-dimensional C concentration profile obtained by atom probe tomography at a total plastic wire deformation strain of ε=2. We observe two distinct regions: (i) From 0 to 20 nm the local C concentration varies around a value of ≈0.1 at.% representing the C background concentration. This value is far above the solubility limit of ferrite at room temperature of $\approx 10^{-10}$ at.%. (ii) From 20 to 30 nm the local C concentration further increases up to 1.5 at.% indicating the presence of a C attractive defect such as a dislocation or a sub-grain boundary. The detailed tomographic results from Ref. [3] suggest that the defect is a 2D defect, possibly a dislocation wall or a low-angle grain boundary. Additional experimental results from Ref. [3] representing the dependence on drawing strain are shown in Fig. 12. The diamonds indicate the average C background concentration and the squares the total C concentration including C atoms at dislocations and sub-grain boundaries. Comparing the C background concentration at ε=2 from Fig. 12 (≈0.2 at.%) we see that it is by a factor of 2 larger than the C background concentration in Fig. 11, indicating a certain scatter in the experimental data.

The experimental C background concentration presented here agrees well with the C concentration increase due to dislocation drag, $\Delta c = 0.15$ at.%, computed in Sec. 3.5. The good agreement should be however taken with care as the computed value is based on a number of simplifying approximations. Additionally, the actual number of C atoms transported from cementite to ferrite must be in fact larger in order to provide the additional C atoms localized in the dislocation cores as discussed further below. Nevertheless, the agreement indicates that dislocation drag is an important kinetic mechanism, contributing to the supersaturation of the ferrite matrix with C atoms during wire drawing of pearlite.

Thermodynamically, C atoms are stabilized in the ferrite matrix by dislocations and by elastic strains (cf. Fig. 4). Elastic strains can be significant during wire drawing and they can critically affect the C formation energy (Fig. 3). Due to the complex microstructure and wire drawing geometry, it is virtually impossible to determine the actual elastic strain level during drawing. However, we can employ an inverse approach to evaluate whether the computed numbers are consistent with experiment. From Fig. 12 we find that the C background concentration increases up to 0.5 at.% for large drawing strains. Using Eq. (9) we can calculate the formation energy required to generate this background concentration in the perfect

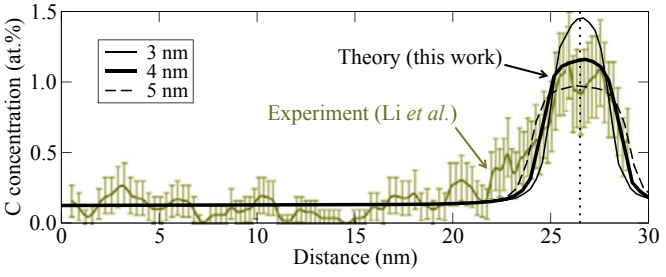

Fig. 11. Local carbon concentration around a defect (marked by the vertical dashed line) in a supersaturated ferrite phase after wire drawing (true strain ε=2). Three theoretical curves (black) are shown corresponding to different averaging box sizes as indicated in the legend. Experimental data (green) are from atom probe tomography measurements as obtained in Ref. [3]. (For interpretation of the references to color in this figure legend, the reader is referred to the web version of this article.)

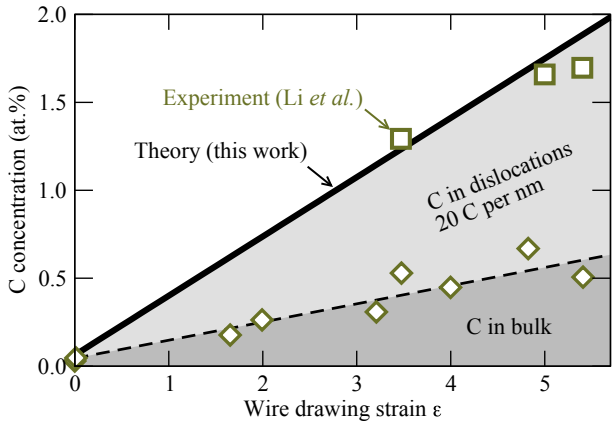

Fig. 12. Total carbon concentration (green squares and solid black line) in the ferrite phase as a function of the true strain due to wire drawing. The green diamonds and the black dashed curve show the experimentally observed and calculated C concentrations, respectively, from the bulk lattice, i.e., excluding the contribution of dislocations. Experimental data are from Ref. [3]. (For interpretation of the references to color in this figure legend, the reader is referred to the web version of this article.)

ferrite phase, resulting in $E_{\text{form}} = 0.16$ eV. From Fig. 3 we see that this formation energy corresponds to an elastic strain of about 1.3%, which is an achievable value at large drawing strains. An important point to note is that—while these elastic strains are predominantly only present during the actual drawing process—they induce, together with the increased C concentration, a mechanically-driven transition to a tetragonally distorted ferrite phase (i.e., martensite) [67], which is responsible for a stabilization of the high C concentration even after the drawing process due to the higher solubility of martensite. Thus, the computed results are consistent with experiment for the C background concentration.

We next investigate whether our theoretical results for the C-dislocation binding energy can help in interpreting the local accumulation of up to 1.5 at.% observed in the experimental data in Fig. 11. For that purpose we use Eq. (9) in combination with the C occupancy limit of 0.04 (= 12 at.%) due to C–C interactions [59] as discussed in Sec. 3.1. For applying Eq. (9) we need the strain dependent formation energy profile $E_{\text{form}}(\varepsilon_{\text{el}})$ for the ferrite bulk *and* the dislocation (Fig. 4). In an ideal case we would employ DFT results due to the discussed quantitative deficiency of the EAM potential in the dislocation core, but computing $E_{\text{form}}(\varepsilon_{\text{el}})$ fully from DFT is computationally prohibitive. At present we can thus only obtain an approximate result based on the EAM energies. Fortunately, the error in the C occupation profile due to the EAM formation energies is not as severe as for the formation energies due to the C–C occupancy limit as estimated at the end of Sec. 3.1. To estimate the effect of the external elastic strain ε_{el}, we adjusted it such as to reproduce the background C concentration in Fig. 11 utilizing the results shown in Fig. 3. The resulting shift was uniformly applied to the full formation energy profile, shifting it down by a constant value of −0.2 eV with respect to the cementite chemical reservoir.

To produce a local C concentration profile representing experimental conditions, we need to integrate the resulting C occupation distribution in boxes of a few nm length. Results for three different box sizes are shown in Fig. 11 by the black curves indicating the sensitivity of the final result with respect to the averaging procedure. The position of the dislocation in our simulation has been adjusted such that the local C increase matches the one obtained from the experimental measurements. This procedure resulted in the dislocation core being placed at the vertical dashed line in Fig. 11.

The resulting good agreement with experimental data requires a careful interpretation due to the fact that the computed profile corresponds to a single dislocation while the experimental data are most probably representing a dislocation wall [3]. A conclusion that can be safely drawn from our theoretical curves is that the extended strain field of the dislocation does not contribute to an increase in the local C concentration because the latter rapidly decreases already within the core region. What really matters for the C concentration increase are the strong C-dislocation binding energies in the dislocation core. From the good agreement between the computed local C concentration around the dislocation and the experimentally measured one we can deduce that quantitatively similar C binding energies are available at the dislocation wall, and that the strain field of the dislocation wall likewise does not significantly contribute to an increase in the local C concentration.

Our theoretical results can be further employed to interpret the total concentration increase in the ferrite phase induced by the wire drawing process (green squares in Fig. 12). To obtain an estimation of the C increase from our results we need the number of C excess atoms per dislocation line length. The latter can be obtained by integrating over the local C concentration (as the one shown in Fig. 11) and subtracting the background bulk concentration. The result depends to some extent on the background concentration, but a value of 20 C/nm reflects a reasonable average value and we use it thus for our estimation. We note that this number, which reflects the number of C excess atoms for a static dislocation, should be distinguished from the numbers (0.01–1 C/nm) obtained in Sec. 3.5, which represent the numbers of C atoms dragged by a mobile dislocation at experimental drawing conditions. To utilize the computed number of C excess atoms for a static dislocation, we additionally need the dislocation density as a function of wire drawing strain for our estimate. For that purpose we parameterize the dislocation density results obtained in Ref. [11] by a linear fit as a function of the drawing strain. Having the C excess per dislocation length unit and the dislocation density we are able to calculate the increase in C concentration in the ferrite phase due to the dislocations. The result is shown in Fig. 12 by the light gray shaded area and adding on top the bulk C concentration (dashed line), we arrive at the total C concentration (solid black curve). We observe a good agreement of our estimate with the experimentally determined concentrations (green squares) thus indicating that dislocations also play an important role in thermodynamically stabilizing the C supersaturation of the ferrite phase during wire drawing.

The analysis here has been based on our results for a screw dislocation. It is conceivable that in the experimental samples dislocations with edge components are likewise present and contribute to the C supersaturation. To estimate the influence of edge dislocations, we can use the results of Veiga et al. [59] who showed that an edge dislocation can store a slightly higher amount of C atoms in the core than a screw dislocation. Thus, in terms of Fig. 11 an edge dislocation would produce a somewhat increased C concentration as compared to the black solid line. Regarding Fig. 12 we can expect that the presence of edge dislocations should increase the number of C excess atoms.

5. Conclusions

We have developed a theoretical multiscale description of the C supersaturation of the ferrite phase in wire drawn pearlite where the C stems from the deformation-driven dissolution of the cementite. Our description is based on atomistic simulations which allowed us to infer the energetic profile of C binding and migration around a screw dislocation in bcc Fe. The computed profile shows specific features in the proximity of the dislocation core which cannot be captured by continuum theory. These energetic features are responsible for a strong binding of C atoms to the dislocation core, but—very remarkably—within the core, the carbon atoms are

rather free to quickly diffuse around due to small energy barriers. Our findings indicate that the previously proposed pipe mechanism for a screw dislocation is unlikely, and instead support the dislocation drag concept for which we proposed a specific drag mechanism, i.e., a mechanism by which mobile dislocations can collect and transport C within their cores from the cementite into the abutting ferrite phase. By employing long time scale diffusion model simulations, we have validated that the atomistically proposed mechanism is indeed realistic also on experimentally relevant time scales.

Applying our results, we could show that the local increase in C concentration in the ferrite phase in severely wire drawn pearlite previously measured by atom probe tomography correlates well with the accumulation of C in the cores of dislocations. The computed profile of the local C concentration allowed us to infer the C excess per dislocation line segment. By combining the computed C excess with previously measured dislocation density data as a function of drawing strain we could compute the total C concentration increase in the ferrite phase. Our results agree well with experimental data and allow us thus to identify dislocations as a main source of C concentration increase during wire drawing of pearlite. We expect this finding to be important, for example, for a further improvement of industrially utilized pearlitic high-strength wires, whose strengthening currently is limited due to a complete decomposition of the cemetite lamellas [9]. The proposed ideas and the developed multiscale methodology will be also applicable to a more general range of nano-crystalline materials produced by severe plastic deformation.

Acknowledgments

We thank S. Goto (Akita University, Japan) and M. Hafez Haghighat (Max-Planck Institut für Eisenforschung, Germany) for discussions on the drag mechanism, E. Kozeschnik (Vienna University of Technology, Austria) for helpful comments on the thermodynamics of carbon, and L. Ventelon (CEA, France) for discussions on the C-dislocation interaction and for providing us the corresponding density-functional-theory results. We also thank R. Spatschek (Max-Planck Institut für Eisenforschung, Germany) for discussions on the diffusion model. This project has received funding from the European Research Council (ERC) under the European Union's Horizon 2020 research and innovation programme (grant agreement No 639211).

References

[1] D. Caillard, An in situ study of hardening and softening of iron by carbon interstitials, Acta Mater. 59 (2011) 4974–4989.
[2] E. Clouet, S. Garruchet, H. Nguyen, M. Perez, C.S. Becquart, Dislocation interaction with C in α-Fe: A comparison between atomic simulations and elasticity theory, Acta Mater. 56 (2008) 3450–3460.
[3] Y. Li, P. Choi, C. Borchers, S. Westerkamp, S. Goto, D. Raabe, R. Kirchheim, Atomic-scale mechanisms of deformation-induced cementite decomposition in pearlite, Acta Mater. 59 (2011) 3965–3977.
[4] A.H. Cottrell, B.A. Bilby, Dislocation theory of yielding and strain ageing of iron, Proc. Phys. Soc. Sect. A 62 (1949) 49–62.
[5] Y. Hanlumyuang, P.A. Gordon, T. Neeraj, D.C. Chrzan, Interactions between carbon solutes and dislocations in bcc iron, Acta Mater. 58 (2010) 5481–5490.
[6] R.G.A. Veiga, M. Perez, C.S. Becquart, E. Clouet, C. Domain, Comparison of atomistic and elasticity approaches for carbon diffusion near line defects in α-iron, Acta Mater. 59 (2011) 6963–6974.
[7] R.G.A. Veiga, M. Perez, C.S. Becquart, C. Domain, S. Garruchet, Effect of the stress field of an edge dislocation on carbon diffusion in α-iron: Coupling molecular statics and atomistic kinetic Monte Carlo, Phys. Rev. B 82 (2010) 054103.
[8] K. Tapasa, Y. Osetsky, D. Bacon, Computer simulation of interaction of an edge dislocation with a carbon interstitial in α–iron and effects on glide, Acta Mater. 55 (2007) 93–104.
[9] Y. Li, D. Raabe, M. Herbig, P.P. Choi, S. Goto, A. Kostka, H. Yarita, C. Borchers, R. Kirchheim, Segregation stabilizes nanocrystalline bulk steel with near theoretical strength, Phys. Rev. Lett. 113 (2014) 106104.
[10] J. Chakraborty, M. Ghosh, R. Ranjan, G. Das, D. Das, S. Chandra, X-ray diffraction and Mössbauer spectroscopy studies of cementite dissolution in cold-drawn pearlitic steel, Philos. Mag. 93 (2013) 4598–4616.
[11] Y.Z. Chen, G. Csiszár, J. Cizek, S. Westerkamp, C. Borchers, T. Ungr, S. Goto, F. Liu, R. Kirchheim, Defects in carbon-rich ferrite of cold-drawn pearlitic steel wires, Metall. Mater. Trans. A 44 (2013) 3882–3889.
[12] S. Goto, R. Kirchheim, T. Al-Kassab, C. Borchers, Application of cold drawn lamellar microstructure for developing ultra-high strength wires, Trans. Nonferrous Metals Soc. China 17 (2007) 1129–1138.
[13] D. Raabe, P. Choi, Y. Li, A. Kostka, X. Sauvage, F. Lecouturier, K. Hono, R. Kirchheim, R. Pippan, D. Embury, Metallic composites processed via extreme deformation: Toward the limits of strength in bulk materials, MRS Bull. 35 (2010) 928–987.
[14] X. Zhang, A. Godfrey, X. Huang, N. Hansen, Q. Liu, Microstructure and strengthening mechanisms in cold–drawn pearlitic steel wire, Acta Mater. 59 (2011) 3422–3430.
[15] M. Zelin, Microstructure evolution in pearlitic steels during wire drawing, Acta Mater. 50 (2002) 4431–4447.
[16] X. Sauvage, J. Copreaux, F. Danoix, D. Blavette, Atomic–scale observation and modelling of cementite dissolution in heavily deformed pearlitic steels, Philos. Mag. A 80 (2000) 781–796.
[17] Y. Li, P. Choi, C. Borchers, Y. Chen, S. Goto, D. Raabe, R. Kirchheim, Atom probe tomography characterization of heavily cold drawn pearlitic steel wire, Ultramicroscopy 111 (2011) 628–632.
[18] S. Goto, R. Kirchheim, T. Al-Kassab, C. Borchers, Application of cold drawn lamellar microstructure for developing ultra-high strength wires, Trans. Nonferrous Metals Soc. China 17 (2007) 1129–1138.
[19] J. Embury, R. Fisher, The structure and properties of drawn pearlite, Acta Metall. 14 (1966) 147–159.
[20] J. Embury, J. Hirth, On dislocation storage and the mechanical response of fine scale microstructures, Acta Metall. Mater. 42 (1994) 2051–2056.
[21] M. Herbig, D. Raabe, Y. Li, P. Choi, S. Zaefferer, S. Goto, Atomic–scale quantification of grain boundary segregation in nanocrystalline material, Phys. Rev. Lett. 112 (2014) 126103.
[22] Y.J. Li, A. Kostka, P. Choi, S. Goto, D. Ponge, R. Kirchheim, D. Raabe, Mechanisms of subgrain coarsening and its effect on the mechanical properties of carbon–supersaturated nanocrystalline hypereutectoid steel, Acta Mater. 84 (2015) 110–123.
[23] R. Naraghi, M. Selleby, J. Ågren, Thermodynamics of stable and metastable structures in Fe–C system, Calphad 46 (2014) 148–158.
[24] V.G. Gavriljuk, Decomposition of cementite in pearlitic steel due to plastic deformation, Mater. Sci. Eng. A 345 (2003) 81–89.
[25] X. Sauvage, Y. Ivanisenko, The role of carbon segregation on nanocrystallisation of pearlitic steels processed by severe plastic deformation, J. Mater. Sci. 42 (2006) 1615–1621.
[26] M. Legros, G. Dehm, E. Arzt, T.J. Balk, Observation of giant diffusivity along dislocation cores, Science 319 (2008) 1646–1649.
[27] E.W. Hart, On the role of dislocations in bulk diffusion, Acta Metall. 5 (1957) 597.
[28] C.S. Becquart, J.M. Raulot, G. Bencteux, C. Domain, M. Perez, S. Garruchet, H. Nguyen, Atomistic modeling of an Fe system with a small concentration of C, Comput. Mater. Sci. 40 (2007) 119–129.
[29] M.I. Mendelev, S. Han, D.J. Srolovitz, G.J. Ackland, D.Y. Sun, M. Asta, Development of new interatomic potentials appropriate for crystalline and liquid iron, Philos. Mag. 83 (2003) 3977–3994.
[30] M. Itakura, H. Kaburaki, M. Yamaguchi, First-principles study on the mobility of screw dislocations in bcc iron, Acta Mater. 60 (2012) 3698–3710.
[31] D.A. Porter, K.E. Easterling, Phase Transformations in Metals and Alloys (Revised Reprint), CRC press, 1992.
[32] G.A. Nematollahi, J. von Pezold, J. Neugebauer, D. Raabe, Thermodynamics of carbon solubility in ferrite and vacancy formation in cementite in strained pearlite, Acta Mater. 61 (2013) 1773–1784.
[33] J.P. Hirth, Dislocation displacement fields in anisotropic media, J. Appl. Phys. 40 (1969) 2177.
[34] S. Plimpton, Fast parallel algorithms for short-range molecular dynamics, J. Comput. Phys. 117 (1995) 1–19.
[35] W. Cai, V. Bulatov, J.-P. Chang, J. L., S. Yip, Dislocation Core Effects on Mobility, in: Dislocations in Solids, 12, Elsevier, 2004.
[36] L. Dezerald, L. Ventelon, E. Clouet, C. Denoual, D. Rodney, F. Willaime, Ab initio modeling of the two-dimensional energy landscape of screw dislocations in bcc transition metals, Phys. Rev. B 89 (2014) 024104.
[37] L. Ventelon, F. Willaime, E. Clouet, D. Rodney, Ab initio investigation of the Peierls potential of screw dislocations in bcc Fe and W, Acta Mater. 61 (2013) 3973–3985.
[38] L. Ventelon, B. Lüthi, E. Clouet, L. Proville, B. Legrand, D. Rodney, F. Willaime, Dislocation core reconstruction induced by carbon segregation in bcc iron, Phys. Rev. B 91 (2015) 220102(R).
[39] L.S.I. Liyanage, S.-G. Kim, J. Houze, S. Kim, M.A. Tschopp, M.I. Baskes, M.F. Horstemeyer, Structural, elastic, and thermal properties of cementite (Fe3C) calculated using a modified embedded atom method, Phys. Rev. B 89 (2014) 094102.
[40] F. Körmann, A. Dick, B. Grabowski, B. Hallstedt, T. Hickel, J. Neugebauer, Free energy of bcc iron: Integrated ab initio derivation of vibrational, electronic, and magnetic contributions, Phys. Rev. B 78 (2008) 033102.

[41] A. Udyansky, J. von Pezold, A. Dick, J. Neugebauer, Orientational ordering of interstitial atoms and martensite formation in dilute Fe–based solid solutions, Phys. Rev. B 83 (2011) 184112.
[42] A. Dick, F. Körmann, T. Hickel, J. Neugebauer, Ab initio based determination of thermodynamic properties of cementite including vibronic, magnetic, and electronic excitations, Phys. Rev. B 84 (2011) 125101.
[43] P.E. Blöchl, Projector augmented-wave method, Phys. Rev. B 50 (1994) 17953–17979.
[44] G. Kresse, J. Furthmüller, Efficient iterative schemes for ab initio total–energy calculations using a plane–wave basis set, Phys. Rev. B 54 (1996) 11169.
[45] G. Kresse, J. Furthmüller, Efficiency of ab-initio total energy calculations for metals and semiconductors using a plane-wave basis set, Comput. Mater. Sci. 6 (1996) 15–50.
[46] G. Kresse, D. Joubert, From ultrasoft pseudopotentials to the projector augmented–wave method, Phys. Rev. B 59 (1999) 1758.
[47] J. Perdew, K. Burke, M. Ernzerhof, Generalized gradient approximation made simple, Phys. Rev. Lett. 77 (1996) 3865–3868.
[48] M. Methfessel, A.T. Paxton, High-precision sampling for Brillouin-zone integration in metals, Phys. Rev. B 40 (1989) 3616–3621.
[49] G. Henkelman, G. Jóhannesson, H. Jónsson, Methods for finding saddle points and minimum energy paths, in: Progress on Theoretical Chemistry and Physics, Kluwer Academic Publishers, 2000, pp. 269–300.
[50] G. Henkelman, H. Jónsson, Improved tangent estimate in the nudged elastic band method for finding minimum energy paths and saddle points, J. Chem. Phys. 113 (2000) 9978.
[51] G. Henkelman, B.P. Uberuaga, H. Jónsson, A climbing image nudged elastic band method for finding saddle points and minimum energy paths, J. Chem. Phys. 113 (2000) 9901–9904.
[52] G.A. Nematollahi, Multiscale Description of Super–saturated Ferrite in Severely Deformed Pearlitic Wires, Ph.D. thesis, Ruhr–Universität, Bochum, 2014.
[53] H. Yoshinaga, S. Morozumi, The solute atmosphere round a moving dislocation and its dragging stress, Philos. Mag. 23 (1971) 1367–1385.
[54] F. Zhang, W.A. Curtin, Atomistically informed solute drag in Al–Mg, Model. Simul. Mater. Sci. Eng. 16 (2008) 055006.
[55] D. Jiang, E. Carter, Carbon dissolution and diffusion in ferrite and austenite from first principles, Phys. Rev. B 67 (2003) 214103.
[56] J.R.G. da Silva, R.B. McLellan, Diffusion of carbon and nitrogen in bcc iron, Mater. Sci. Eng. 26 (1976) 83.
[57] D. Caillard, Kinetics of dislocations in pure Fe. part ii. in situ straining experiments at low temperature, Acta Mater. 58 (2010) 3504–3515.
[58] D. Caillard, Kinetics of dislocations in pure Fe. part i. in situ straining experiments at room temperature, Acta Mater. 58 (2010) 3493–3503.
[59] R.G. Veiga, M. Perez, C.S. Becquart, C. Domain, Atomistic modeling of carbon Cottrell atmospheres in bcc iron, J. Phys. Condens. Matter 25 (2013) 025401.
[60] Y. Li, P. Choi, S. Goto, C. Borchers, D. Raabe, R. Kirchheim, Evolution of strength and microstructure during annealing of heavily cold-drawn 6.3 GPa hypereutectoid pearlitic steel wire, Acta Mater. 60 (2012) 4005–4016.
[61] H. Schultz, Point defects in body–centered cubic transition metals, Mater. Sci. Eng. 3 (1968) 189.
[62] D. Simonovic, C.K. Ande, A.I. Duff, F. Syahputra, M.H.F. Sluiter, Diffusion of carbon in bcc Fe in the presence of Si, Phys. Rev. B 81 (2010) 054116.
[63] D.A. Porter, K.E. Easterling, G.D.W. Smith, Dynamic studies of the tensile deformation and fracture of pearlite, Acta Metall. 26 (1978) 1405–1422.
[64] F. R. Nabarro, Report of a Conference on Strength of Solids, The Physical Society, London 75.
[65] P.D. Ispánovity, I. Groma, G. Györgyi, F.F. Csikor, D. Weygand, Submicron plasticity: Yield stress, dislocation avalanches, and velocity distribution, Phys. Rev. Lett. 105 (2010) 085503.
[66] S. Goto, private communication.
[67] S. Djaziri, Y. Li, A. Nematollahi, B. Grabowski, S. Goto, C. Kirchlechner, J. Neugebauer, D. Raabe, G. Dehm, (submitted) for publication.